

Large-area and high-quality 2D transition metal telluride

Jiadong Zhou^{1†}, Fucai Liu^{1†}, Junhao Lin^{2,3,4*}, Xiangwei Huang^{5†}, Juan Xia⁶, Bowei Zhang¹, Qingsheng Zeng¹, Hong Wang¹, Chao Zhu¹, Lin Niu¹, Xuewen Wang¹, Wei Fu¹, Peng Yu¹, Tay-Rong Chang⁷, Chuang-Han Hsu^{8,9}, Di Wu^{8,9}, Horng-Tay Jeng^{7,10}, Yizhong Huang¹, Hsin Lin^{8,9}, Zexiang Shen^{1,6,11}, Changli Yang^{5,12}, Li Lu^{5,12}, Kazu Suenaga⁴, Wu Zhou², Sokrates T. Pantelides^{2,3}, Guangtong Liu^{5*} and Zheng Liu^{1, 13,14*}.

¹Centre for Programmable Materials, School of Materials Science and Engineering, Nanyang Technological University, Singapore 639798, Singapore

²Materials Science and Technology Division, Oak Ridge National Lab, Oak Ridge Tennessee 37831, USA

³Department of Physics and Astronomy, Vanderbilt University, Nashville, TN 37235, USA

⁴National Institute of Advanced Industrial Science and Technology (AIST), Tsukuba 305-8565, Japan

⁵Beijing National Laboratory for Condensed Matter Physics, Institute of Physics, Chinese Academy of Sciences, Beijing 100190, China

⁶Division of Physics and Applied Physics, School of Physical and Mathematical Sciences, Nanyang Technological University, Singapore 637371, Singapore

⁷Department of Physics, National Tsing Hua University, Hsinchu 30013, Taiwan

⁸Centre for Advanced 2D Materials and Graphene Research Centre, National University of Singapore, Singapore 117546

⁹Department of Physics, National University of Singapore, Singapore 117542

¹⁰Institute of Physics, Academia Sinica, Taipei 11529, Taiwan

¹¹Centre for Disruptive Photonic Technologies, School of Physical and Mathematical Sciences, Nanyang Technological University, Singapore 637371, Singapore

¹²Collaborative Innovation Center of Quantum Matter, Beijing 100871, China

¹³Centre for Micro-/Nano-electronics (NOVITAS), School of Electrical & Electronic Engineering, Nanyang Technological University, 50 Nanyang Avenue, Singapore 639798, Singapore

¹⁴CINTRA CNRS/NTU/THALES, UMI 3288, Research Techno Plaza, 50 Nanyang Drive, Border X Block, Level 6, Singapore 637553, Singapore

† These authors contributed equally to this work. Correspondence and requests for materials should be addressed to J.L (email:lin.junhao@aist.go.jp), G.L (email:gqliu@iphy.ac.cn) and Z.L. (email:z.liu@ntu.edu.sg)

Abstract

Atomically thin transitional metal ditellurides like WTe_2 and MoTe_2 have triggered tremendous research interests because of their intrinsic nontrivial band structure. They are also predicted to be 2D topological insulators and type-II Weyl semimetals. However, most of the studies on ditelluride atomic layers so far rely on the low-yield and time-consuming mechanical exfoliation method. Direct synthesis of large-scale monolayer ditellurides has not yet been achieved. Here, using the chemical vapor deposition (CVD) method, we demonstrate controlled synthesis of high-quality and atom-thin tellurides with lateral size over $300\ \mu\text{m}$. We found that the as-grown WTe_2 maintains two different stacking sequences in the bilayer, where the atomic structure of the stacking boundary is revealed by scanning transmission electron microscope (STEM). The low-temperature transport measurements revealed a novel semimetal-to-insulator transition in WTe_2 layers and an enhanced superconductivity in few-layer MoTe_2 . This work paves the way to the synthesis of atom-thin tellurides and also quantum spin Hall devices.

Introduction

Distinct from most semiconducting transition-metal sulfide and selenide compounds that are only stable in the 2H phase, tellurides exhibit much richer structural variations and electronic properties, from semiconducting in the 2H phase to semi-metallic in the $1\text{T}'$ phase. Among all telluride compounds, MoTe_2 crystal is stable in both 2H and $1\text{T}'$ phase while WTe_2 only form $1\text{T}'$ phase in nature (Fig. 1a). Therefore, transition metal ditellurides, represented by MoTe_2 and WTe_2 , have attracted tremendous interests recently due to the facile switching between different phases and their unique electronic properties. For instance, large and non-saturating magnetoresistance in WTe_2 bulk crystal was reported by Ali *et al*(1), presumably due to the perfect compensation of the electrons and holes even in an ultrahigh magnetic field. A laser-induced transition between 2H and $1\text{T}'$ phases in MoTe_2 thin film has been demonstrated to show an Ohmic homojunction(2). Furthermore, high mobility up to $4000\ \text{cm}^2/\text{Vs}$ and $10000\ \text{cm}^2/\text{Vs}$ were reported in MoTe_2 and WTe_2 , respectively (3, 4). MoTe_2 and WTe_2 atomic layers are also predicted to be promising

candidates of type-II Weyl semimetals (5, 6), even in their alloys 1T' (W, Mo)Te₂ (7). More importantly, monolayer tellurides like WTe₂ and MoTe₂ are predicted to be a 2D topological insulator(8). These make transition metal ditellurides an excellent platform for studying fundamental physical phenomena, such as superconductivity(9) and quantum spin Hall effect(8). They are also promising candidates for various potential applications such as spintronics and high-efficiency thermoelectric devices (10, 11).

However, most of the novel physical phenomena in transition-metal ditellurides have been demonstrated in mechanically exfoliated layers, e.g., the magnetoresistance in few-layer WTe₂(4) and the superconductivity in bulk 1T'-MoTe₂(12). The exfoliation method is low-yield and time-consuming and only good for scientific research. Direct synthesis of few-layer and monolayer ditelluride would, therefore, be essential to large-scale applications. Among all the growth techniques, chemical vapor deposition (CVD) has been demonstrated as a facile method in synthesizing monolayer crystals in large scale, including graphene(13), MoS₂/WS₂(14, 15), MoSe₂/WSe₂(16, 17), and their heterojunctions(18-20), by using different precursors under optimized reaction conditions. Although telluride compounds such as MoTe₂ films were successfully synthesized by thermal flux and tellurization of molybdenum films(3, 21), controlled synthesis of high-quality telluride atomic layers, even down to monolayer, remains elusive under the existing CVD or physical vapor deposition (PVD) conditions, mainly due to the lower environmental stability and activity of tellurium. For instance, the low chemical reaction activity of W and Mo with Te limits tellurization of W and Mo precursors (powder and oxides), although this method has been widely adopted for the preparation of sulfide and selenide monolayers. More specifically, the electronegativity difference between transitional metal (W or Mo) and Te is very small (~ 0.4 eV or 0.3 eV), indicating a weak bonding between the metals and Te atoms which

makes the stoichiometry of ditellurides difficult to be obtained. Furthermore, even though the stoichiometry of WTe_2 and MoTe_2 is maintained, the as-synthesized product tends to decompose rapidly by emitting Te vapor at high reaction temperature (around 600 °C)(10), instead of evaporating into gas-phase telluride.

Here, we demonstrate a CVD strategy to directly synthesize WTe_2 and MoTe_2 few-layer and monolayers at large scale. The mixed compounds (weight ratio of the compound metal oxide: metal chlorides: Te is 1:1:1) and Te were used as the source of W (Mo) and Te, respectively. Such configuration of the precursors makes the reaction between Te and the metal sources react easily. The Te in the mixed compounds can decrease the melting point of the mixed compounds, while the other Te powder in the upstream was used as to keep the Te atmosphere in the whole reaction process. The corresponding chemical reaction is shown in Supplementary Information. Raman spectroscopy was used to characterize the quality of the WTe_2 and MoTe_2 flakes to confirm their high quality. Two different stacking sequences of WTe_2 bilayers were observed by STEM. The as-grown WTe_2 atomic layers show non-saturating magnetoresistance which resembles the features of the mechanical exfoliated ones. A novel semimetal-to-insulator transition is observed in the electrical measurements of WTe_2 few layers, whereas the few-layer MoTe_2 shows enhanced superconducting behavior.

Results

Side view and top view of the crystal structure of $1T'$ WTe_2 and MoTe_2 is shown in Fig. 1a and 1b, respectively. A schematic diagram of the reaction system is shown in Supplementary Fig. S1. The reaction temperature is between 750 ~ 850 °C (see Methods). The thickness of the WTe_2 and MoTe_2 atomic layers can be controlled by the growth time. Single crystalline monolayer WTe_2 can be consistently obtained in 5 min at 820 °C with specific flow amount of carrier gas (100 sccm

Ar/15 sccm H₂), while increasing the reaction time results in thick WTe₂ flakes. Optical and atomic force microscopy (AFM) images of WTe₂ flakes with different thicknesses are shown in Fig. S2 and S3, respectively. Figure 1c shows a single-crystalline monolayer WTe₂ with a length of ~ 350 μm and width of ~ 20 μm. The sharp edges at the two ends of this rectangle suggest the edge of WTe₂ in 1T' phase is terminated by planes that are intersected by 50°. Figure 1d shows the optical image of a polycrystalline WTe₂ monolayer film with domain size exceeding 100 μm. Figure 1e shows a bilayer WTe₂ with a grain boundary at the intersection of two rectangular WTe₂ domains (center of the image), as highlighted by the dashed line. For better visibility, the grain boundary with contrast enhancement and false color is shown in the inset of Fig. 1e. The SEM images of WTe₂ films are shown in Supplementary Fig. S4. Under similar conditions, ribbon-like monolayer 1T' MoTe₂ up to 150 μm (Fig. 1f) and few layered 1T' MoTe₂ up to 200 μm (Fig. 1g) are also obtained by controlling the Te source according to the phase diagram(3). Unlike WTe₂, different number of layers can be found in the same flake, as shown in Fig. 1g, where monolayer (1L), bilayer (2L) and trilayer (3L) MoTe₂ are clearly distinguished by sharp contrast. Atomic force microscopy (AFM) and SEM images of MoTe₂ flakes are shown in Supplementary Fig. S5 and S6, respectively.

Raman spectroscopy was employed to characterize the quality of the WTe₂ and MoTe₂ atomic layers. Figure 2a shows the Raman spectra of WTe₂ films with different thicknesses ranging from monolayer to bulk. For few-layer WTe₂ (< 10 L), only four optical vibrational modes, namely B_1^{10} , A_2^3 , A_1^7 and A_1^9 were identified, compared with that reported in WTe₂ crystal and flakes(22, 23). Interestingly, the B_1^{10} mode was not reported in few-layer WTe₂. Furthermore, the intensity of A_1^7 peak becomes stronger than other modes as the layer number decreases, similar to the reported result that collected the Raman spectra along *b* axis of the mechanically exfoliated WTe₂ atomic

layer(24). These results further confirm the high quality of our as-synthesized WTe₂ atomic layers. The optical image and Raman intensity mapping (A_1^g , $\sim 205\text{ cm}^{-1}$) of WTe₂ is shown in Fig. 2b and 2c, respectively. The region for Raman mapping is highlighted in blue dashed square and the mapping size is around $20\times 20\ \mu\text{m}$. Raman mapping shows homogeneous intensity across the whole region, which indicates a low defect concentration in the as-synthesized WTe₂ monolayers. We also find that the grain boundary in WTe₂ can be easily distinguished from the nearby regions in the Raman intensity mapping (Supplementary information Fig. S7). Monolayer and few-layer Raman spectra contour map of MoTe₂ is shown in Fig. 2d. The Raman peaks in monolayer were observed at 127, 161, 189 and 267 cm^{-1} , corresponding to the Raman-active A_g modes of monolayer MoTe₂ in 1T' phase (25) (Supplementary information Fig. S8). The spectrum agrees well with the previous reported result (3, 21, 26). The Raman spectrum of 2H and 1T' MoTe₂ synthesized by controlling the Te source are shown in Supplementary information Fig. S8. Figure 2e shows a typical optical image of 1T' MoTe₂ few layers. Raman intensity mapping was collected at the region highlighted by the blue dashed square. Due to the high contrast, monolayer and bilayer MoTe₂ can be easily differentiated from Raman mapping (Fig. 2f). In addition to Raman characterization, X-ray photoelectron spectroscopy (XPS) was used to analyze the elemental distribution of WTe₂ and MoTe₂ atomic layers. The ratio of transition metals (W or Mo) and Te were found to be very close to 1:2, in good agreement with the stoichiometry of WTe₂ and MoTe₂, as shown in Supplementary Fig. S9.

Atom-resolved scanning transmission electron microscope (STEM) was applied to further investigate the atomic structure of the as-synthesized MoTe₂ and WTe₂ atomic layers. Figure 3a shows a high-resolution Z-contrast STEM image of a monolayer WTe₂, revealing the 1T' phase which composes of quasi-one-dimensional tungsten-tellurium zigzag chains along the a axis of the

unit cell (highlighted by the dashed white rectangle) and connected by Te atoms in between, as indicated in the overlaid atomic structural model. The connected Te atoms can also be viewed as a Te chain parallel to the W-Te chains. The Fast Fourier transformation (FFT) pattern shown in the inset further confirms the rectangular shape of the WTe_2 unit cell. Figure 3b shows a line intensity profile along the b axis of the crystal, indicating two distinct positions for Te atoms bonding to the W atom in the distorted 1T phase, with a measured distance of 2.49 Å and 1.61 Å, respectively. The simulated STEM image using the overlaid atomic structural model achieves a good agreement with the experimental image, as shown in the inset of Fig. 3a. TEM characterization on thick flakes WTe_2 is shown in Supplementary Fig. S10, further confirming the high quality of the sample.

The as-synthesized $MoTe_2$ atomic layer also maintains the 1T' phase similar to the WTe_2 layer presented above, as shown in Supplementary Fig. S11, where the electron-energy-loss spectra (EELS) are provided for direct comparison between the two materials. In light of the co-existence of different stacking orders in 2D materials, we also found that the CVD-grown 1T' WTe_2 maintains two different stacking sequences in the bilayer that are similar to other 2D materials. Fig. 3c and 3d show the atomic structures of two WTe_2 bilayer regions, which are distinguishable from each other. Specifically, Figure. 3c shows a bilayer stacking where the second layer is mirror symmetric to the first layer along the b axis of the WTe_2 unit cell, as shown by the opposite orientations of the two layers in the top view of the structural model (the dashed diamonds). The Te chains of the second layer aligns with the W-Te zigzag chains of the first layer vertically, and vice versus, which can be visualized in the side view of the structural model. Such kind of stacking is similar to the 2H stacking in TMDs and AA' stacking in h-BN. Therefore, we called it 2H stacking following the convention. Figure 3d shows another stacking pattern of WTe_2 , where the

second layer shifts half of a unit cell along the b axis away from the 2H stacking shown in Fig. 3c, as indicated by the structural model. We called such stacking 2H' stacking. Both stackings form periodic stripe patterns, which consist of overlapped Te and W-Te chains from the two layers, in good agreement with the simulated STEM images (Supplementary information Fig. S12). Density functional theory (DFT) calculations on the 2H and 2H' stacking show very similar band structure, both of which maintain semi-metallic properties, as shown in Supplementary Fig. S13. Interlayer shifting along b axis(27), however, is rarely observed in WTe₂, presumably due to the large interlayer interaction in materials composed by heavy elements. Figure 3e shows an atomically sharp stacking boundary between the 2H and 2H' stacking domains, as highlighted by the green dashed rectangle. A simulated STEM image based on the DFT-relaxed model between the two stackings is shown in supplementary Fig. S13, which resembles most feature of the stacking boundary observed experimentally. Due to the symmetry of the zigzag chains, the second layers in the two stacking form are also mirror symmetric to each other which forms a mirror twin boundary, similar to the graphene domain wall(28). DFT calculations further indicate the Te₂ columns are misaligned in the relaxed structure of the mirror twin boundary (inset in Fig. 3f), different from those observed in other TMDs(29-31). A projected density of states (DOS) illustrates (Fig. 3f) that the W atoms in the mirror twin boundary show more states at the Fermi level, suggesting they are more metallic than the bulk counterpart, which may have important contributions in the electrical behavior to the monolayer and few-layer WTe₂ and also implications on the quantum spin Hall effect in WTe₂.

Layered CVD-grown ditelluride films provide an excellent platform to study the thickness-dependent electric transport. The electrical properties of the as-synthesized WTe₂ and MoTe₂ flakes with different thickness were investigated by means of field- and temperature-dependent

transport measurements, as shown in Fig. 4. Figure 4a shows the resistivity of WTe₂ as a function of temperature with thickness of 4 nm (5 layer), and 2 nm (2 layer). The corresponding optical and AFM images of the WTe₂ devices are shown in Supplementary Fig. S14. Above 50 K, the resistance of 4 nm WTe₂ decreasing monotonically with decreasing temperature shows a metallic behavior, which is similar to the transport properties of the bulk WTe₂. However, an upturn in resistance curve was observed with T further reduced. Such phenomenon may be due to the two-dimensional electron-electron interactions at the reduced dimension (32). Interestingly, the bilayer WTe₂ (with thickness of 2 nm) displays solely insulating behavior under zero magnetic field, confirming that the semimetal-to-insulator transition originates from the effect of the reduced thickness. Such phenomenon has been observed in mechanically exfoliated WTe₂ few layers, where the insulating state may be attributed to the Anderson localization in the two dimensional limit(4). The temperature-dependent magnetoresistance (MR) calculated by $MR=[\rho(H)-\rho(0)]/\rho(0)$ of bilayer WTe₂ as a function of the magnetic field is shown in Fig. 4b. These results show that large and non-saturating magnetoresistance is preserved in our CVD-grown WTe₂ even down to a bilayer sample, which further demonstrates their high quality. The MR reaches a maximum value of 28% at 2 K. For the thick WTe₂ flakes (12 nm), the MR is about 2000% at 25K in a field of 10T, which is shown in Supplementary Fig. S15. These values are close to the order of magnitude of the recent reports(4).

Enhanced superconductivity is also observed in our as-synthesized few-layer MoTe₂. The optical image of the MoTe₂ device is shown in Supplementary Fig. S16. Figure 4c shows the longitudinal resistance R_{xx} as a function of temperature T of few-layer MoTe₂ device in different perpendicular magnetic fields. R_{xx} decreases steadily from 300K to 40K, indicating that the sample shows a metallic behavior which is consistent with previous studies on exfoliated samples (3). With T

further reduced, the sample gradually becomes superconducting below $T=2.5\text{K}$ (the onset of transition) and reaches zero resistance at $T_c=0.5\text{K}$. Surprisingly, the superconductivity in thinner samples is strongly enhanced compared with $T_c=0.1\text{K}$ reported in its bulk counterpart (12). A similar phenomenon was observed in 2H TaS₂(33), and the reason is ascribed to an enhancement of the effective electron–phonon coupling constant in thinner samples. The inset of Fig. 4c displays the longitudinal resistance R_{xx} as a function of temperature in different perpendicular magnetic fields. We define the superconducting transition temperature T_c under different magnetic fields as the temperature at which the resistance drops to 10% of the normal state resistance R_N . T_c shifts systematically to lower temperatures with increasing magnetic fields B . Finally, the superconductivity was completely suppressed when $B\geq 1\text{T}$. We summarize the upper critical field H_{c2} - T_c phase diagram in Fig. 4d and find a linear relationship between H_{c2} and T_c near T_c . This is a characteristic of 2D superconductors and can be explained by the standard linearized Ginzburg-Landau (GL) theory,

$$H_{c2}(T) = \frac{\phi_0}{2\pi\xi_{GL}(0)^2} \left(1 - \frac{T}{T_c}\right)$$

where $\xi_{GL}(0)$ is the zero-temperature GL in-plane coherence length and ϕ_0 is the magnetic flux quantum. By fitting the experimental data with the above formula, a coherence length of 38 nm was obtained, which is much larger than that in Mo₂C(34).

Discussion

In summary, large-scale and atom-thin ditellurides including WTe₂ and MoTe₂ were synthesized. Complementary characterizations demonstrated the high quality of as-grown samples. High-resolution STEM imaging resolved that atomic structure of WTe₂ and MoTe₂ and also observed the domain wall in bi-layer WTe₂ where the stacking boundary are revealed between two distinct

stacking sequences. Electric transport measurement also revealed the semimetal-to-insulator transition in WTe_2 and enhanced superconductivity in MoTe_2 . Our work will shed light on the synthesis of atom-thin telluride materials and boost the realization of quantum spin Hall devices.

Materials and Methods

Synthesis of MoTe_2 and WTe_2 . The WTe_2 (MoTe_2) crystals were synthesized by CVD method using WO_3 (MoO_3) and WCl_6 (MoCl_5) (Sigma) as the W sources. The Te powder was used as the Te sources. The crystals are synthesized in quartz tube (1 inch diameter) with temperature from 700 to 850 °C. The system of the reaction is shown in Supplementary Fig. S1. Specifically, for the WTe_2 , the mixed gas of H_2/Ar with 15 sccm and 150 sccm were used as the carrier gas, the silicon boat contained 30 mg mixed powders with WO_3 : WCl_6 : $\text{Te}=1:1:1$ (weight ratio) was put in the center of the tube. The SiO_2/Si substrate is placed downstream. Another silicon boat containing 0.5 g Te powder is put on the upstream. The temperature ramps up to the 820 °C in 17 min, and keeping at the reaction temperature for about 5 min to 15 min. Then the furnace cools down to room temperature gradually. For the MoTe_2 , the mixed gas of H_2/Ar with 15 sccm and 200 sccm were used as the carrier gas, the silicon boat contained 30mg mixed powder with MoO_3 : MoCl_5 : $\text{Te}=1:1:1$ was put in the center of the tube. The SiO_2/Si substrate is placed downstream. Another silicon boat contained 0.5 g Te powders is put on the upstream. The temperature ramps up to the 780 °C in 16 min, and keeping at the reaction temperature for about 5 min to 15 min. Then the furnace cools down to room temperature gradually. Detailed description of the growth is given in supporting Supplementary Information.

Raman Characterization. Raman measurements with an excitation laser of 532 nm was performed using a WITEC alpha 200R Confocal Raman system. Before Raman characterization, the system was calibrated with the Raman peak of Si at 520 cm^{-1} . The laser powers are less than 1mW to avoid overheating of the samples.

TEM and STEM Characterization. The STEM samples were prepared with a poly (methyl methacrylate) (PMMA) assisted method. A layer of PMMA of about $1\text{ }\mu\text{m}$ thick was spin-coated on the wafer with WTe_2 (MoTe_2) samples deposited, and then baked at $180\text{ }^\circ\text{C}$ for 3min. Afterwards, the wafer was immersed in NaOH solution (1M) to etch the SiO_2 layer over night. After lift-off, the PMMA/ WTe_2 (MoTe_2) film was transferred into DI water for several cycles to wash away the residual contaminants, and then it was fished by a TEM grid (Quantifoil Mo grid). The transferred specimen was dried naturally in ambient environment, and then dropped into acetone overnight to wash away the PMMA coating layers. The STEM imaging shown in the main text was performed on an aberration-corrected Nion UltraSTEM-100 operating at 100 kV. The convergence semi-angle for the incident probe was 31 mrad. Z-contrast images were collected for a half-angle range of $\sim 86\text{-}200$ mrad. STEM imaging and EELS analysis on MoTe_2 shown in the SI were performed on a JEOL 2100F with a cold field-emission gun and an aberration corrector (the DELTA-corrector) operating at 60 kV. A Gatan GIF Quantum was used for recording the EELS spectra. The inner and outer collection angles for the STEM image (β_1 and β_2) were 62 and $129\text{-}140$ mrad, respectively, with a convergence semi-angle of 35 mrad. The beam current was about 15 pA for the ADF imaging and EELS chemical analyses. All imaging was performed at room temperature.

Devices fabrication and transport measurement. The Hall bar are patterned on few layer MoTe_2 and WTe_2 using e-beam lithography. The Ti/Au (5/50 nm) electrodes are deposited using the

thermal evaporator, followed by the lift off process. For the measurements of WTe₂, the transport measurement is performed in the Quantum Design PPMS system with temperature ranging from 300 K to 2 K, and magnetic field up to 14 T. For the superconductivity measurements of MoTe₂, the transport experiment is carried out in a top-loading Helium-3 cryostat in a superconducting magnet. An ac probe current $I_{ac}=10$ nA at 30.9 Hz is applied from the source to the drain. Then a lock-in amplifier monitors the longitudinal R_{xx} through two additional electrical contacts.

Supplementary Materials

Fig. S1. Synthesis of WTe₂ and MoTe₂ films

Fig. S2. Optical images of WTe₂ flakes with different thickness

Fig. S3. AFM measurements of WTe₂ flakes

Fig. S4. SEM images of WTe₂ films

Fig. S5. AFM measurement of monolayer MoTe₂

Fig. S6. Morphologies of monolayer, bilayer and trilayer MoTe₂

Fig. S7. The Raman mapping of WTe₂

Fig. S8. Raman spectra of 2H and 1T' MoTe₂

Fig. S9. XPS test of the monolayer WTe₂ and MoTe₂

Fig. S10. TEM characterize of WTe₂ flakes

Fig. S11. Atomic structure of MoTe₂ and WTe₂ few layers

Fig. S12. Simulated STEM image of the stacking boundary in WTe₂ bilayer

Fig. S13. Crystal and band structures of monolayer and bilayer WTe₂

Fig. S14. AFM images of the WTe₂ flakes used in the devices

Fig. S15. Magnetoresistance of thick WTe₂ flakes

Fig. S16. Optical image of MoTe₂ device

Reference:

1. M. N. Ali *et al.*, Large, non-saturating magnetoresistance in WTe₂. *Nature* **514**, 205-208 (2014).
2. S. Cho *et al.*, Phase patterning for ohmic homojunction contact in MoTe₂. *Science* **349**, 625-628 (2015).
3. D. H. Keum *et al.*, Bandgap opening in few-layered monoclinic MoTe₂. *Nat Phys* **11**, 482-486 (2015).
4. L. Wang *et al.*, Tuning magnetotransport in a compensated semimetal at the atomic scale. *Nat Commun* **6**, 8892 (2015).
5. A. A. Soluyanov *et al.*, Type-II Weyl semimetals. *Nature* **527**, 495-498 (2015).
6. Y. Sun, S. C. Wu, M. N. Ali, C. Felser, B. H. Yan, Prediction of Weyl semimetal in orthorhombic MoTe₂. *Phys Rev B* **92**, 161107 (2015).
7. T. R. Chang *et al.*, Prediction of an arc-tunable Weyl Fermion metallic state in Mo_xW_{1-x}Te₂. *Nat Commun* **7**, 10639 (2016).
8. X. F. Qian, J. W. Liu, L. Fu, J. Li, Quantum spin Hall effect in two-dimensional transition metal dichalcogenides. *Science* **346**, 1344-1347 (2014).
9. D. F. Kang *et al.*, Superconductivity emerging from a suppressed large magnetoresistant state in tungsten ditelluride. *Nat Commun* **6**, 7804 (2015).
10. J. E. Callanan, G. A. Hope, R. D. Weir, E. F. Westrum, Thermodynamic Properties of Tungsten Ditelluride (WTe₂) .1. The Preparation and Low-Temperature Heat-Capacity at Temperatures from 6-K to 326-K. *J Chem Thermodyn* **24**, 627-638 (1992).
11. P. A. G. Ohare, G. A. Hope, Thermodynamic Properties of Tungsten Ditelluride (WTe₂) .2. Standard Molar Enthalpy of Formation at the Temperature 298.15-K. *J Chem Thermodyn* **24**, 639-647 (1992).
12. Y. P. Qi *et al.*, Superconductivity in Weyl semimetal candidate MoTe₂. *Nat Commun* **7**, 11038 (2016).
13. T. R. Wu *et al.*, Fast growth of inch-sized single-crystalline graphene from a controlled single nucleus on Cu-Ni alloys. *Nat Mater* **15**, 43-47 (2016).
14. Y. Gao *et al.*, Large-area synthesis of high-quality and uniform monolayer WS₂ on reusable Au foils. *Nat Commun* **6**, 8569 (2015).
15. S. Najmaei *et al.*, Vapour phase growth and grain boundary structure of molybdenum disulphide atomic layers. *Nat Mater* **12**, 754-759 (2013).
16. J. K. Huang *et al.*, Large-Area Synthesis of Highly Crystalline WSe₂ Mono layers and Device Applications. *Acs Nano* **8**, 923-930 (2014).
17. X. L. Wang *et al.*, Chemical Vapor Deposition Growth of Crystalline Mono layer MoSe₂. *Acs Nano* **8**, 5125-5131 (2014).
18. Y. J. Gong *et al.*, Vertical and in-plane heterostructures from WS₂/MoS₂ monolayers. *Nat Mater* **13**, 1135-1142 (2014).
19. C. M. Huang *et al.*, Lateral heterojunctions within monolayer MoSe₂-WSe₂ semiconductors. *Nat Mater* **13**, 1096-1101 (2014).
20. M. Y. Li *et al.*, Epitaxial growth of a monolayer WSe₂-MoS₂ lateral p-n junction with an atomically sharp interface. *Science* **349**, 524-528 (2015).
21. J. C. Park *et al.*, Phase-Engineered Synthesis of Centimeter-Scale 1T'- and 2H-Molybdenum Ditelluride Thin Films. *Acs Nano* **9**, 6548-6554 (2015).
22. M. K. Jana *et al.*, A combined experimental and theoretical study of the structural, electronic and vibrational properties of bulk and few-layer Td-WTe₂. *J Phys-Condens Mat* **27**, 285401 (2015).
23. Y. Kim *et al.*, Anomalous Raman scattering and lattice dynamics in mono- and few-layer WTe₂. *Nanoscale* **8**, 2309-2316 (2016).

24. Y. C. Jiang, J. Gao, L. Wang, Raman fingerprint for semi-metal WTe₂ evolving from bulk to monolayer. *Sci Rep* **6**, 19624 (2016).
25. M. Kan, H. G. Nam, Y. H. Lee, Q. Sun, Phase stability and Raman vibration of the molybdenum ditelluride (MoTe₂) monolayer. *Phys Chem Chem Phys* **17**, 14866-14871 (2015).
26. L. Zhou *et al.*, Large-Area Synthesis of High-Quality Uniform Few-Layer MoTe₂. *J Am Chem Soc* **137**, 11892-11895 (2015).
27. X. Lu *et al.*, Rapid and Nondestructive Identification of Polytypism and Stacking Sequences in Few-Layer Molybdenum Diselenide by Raman Spectroscopy. *Adv Mater* **27**, 4502-4508 (2015).
28. L. Brown *et al.*, Twinning and Twisting of Tri- and Bilayer Graphene. *Nano Lett* **12**, 1609-1615 (2012).
29. X. Lu *et al.*, Large-Area Synthesis of Monolayer and Few-Layer MoSe₂ Films on SiO₂ Substrates. *Nano Lett* **14**, 2419-2425 (2014).
30. A. M. van der Zande *et al.*, Grains and grain boundaries in highly crystalline monolayer molybdenum disulphide. *Nat Mater* **12**, 554-561 (2013).
31. J. H. Lin, S. T. Pantelides, W. Zhou, Vacancy-Induced Formation and Growth of Inversion Domains in Transition-Metal Dichalcogenide Monolayer. *Acs Nano* **9**, 5189-5197 (2015).
32. J. Hu *et al.*, Enhanced electron coherence in atomically thin Nb₃SiTe₆. *Nat Phys* **11**, 471-476 (2015).
33. E. Navarro-Moratalla *et al.*, Enhanced superconductivity in atomically thin TaS₂. *Nat Commun* **7**, 11043 (2016).
34. C. Xu *et al.*, Large-area high-quality 2D ultrathin Mo₂C superconducting crystals. *Nat Mater* **14**, 1135-1141 (2015).

Acknowledgements

This work is supported by the Singapore National Research Foundation under NRF RF Award No. NRF-RF2013-08, the start-up funding from Nanyang Technological University (M4081137.070). JL and KS acknowledge support from the JST Research Acceleration Programme. This research was also supported in part by U.S. DOE grant DE-FG02-09ER46554 (JL, STP), by the U.S. Department of Energy, Office of Science, Basic Energy Science, Materials Sciences and Engineering Division (WZ), and through a user project at ORNL's Center for Nanophase Materials Sciences (CNMS), which is a DOE Office of Science User Facility. This research used resources of the National Energy Research Scientific Computing Center, which is supported by the Office of Science of the US Department of Energy under Contract No. DE-AC02-05CH11231. T.R.C. and H.T.J. are supported by the Ministry of Science and Technology, National Tsing Hua University, and Academia Sinica, Taiwan. We also thank NCHC, CINC-NTU and NCTS, Taiwan for technical

support. H.L. acknowledges the Singapore National Research Foundation for the support under NRF Award No. NRF-NRFF2013-03. The work at IOP was supported by the National Basic Research Program of China from the MOST under the grant No.2014CB920904 and 2013CB921702, by the NSFC under the grant No. 11174340 and 91421303.

Additional information competing financial interests: The authors declare no competing financial interests.

Author contributions

J.Z., Z.L. designed the experiments. J.Z worked on the growth of WTe₂ and MoTe₂. J.X. and J.Z. carried out Raman characterizations and analyzed the data. J.L. performed all the STEM characterization of the samples and analysis. T.R.C., C.-H.C, D.W., H.T.J, and H.L. performed electronic structure calculations. B,Z. performed the TEM of thick WTe₂ flakes. J.Z. performed the AFM test. F.L fabricated and measured the WTe₂ devices. Q,Z. and C,Z. fabricated the MoTe₂ devices. X.H. measured the superconductivity in MoTe₂. J.Z., J.L. and Z.L. wrote the paper. All authors discussed and commented on the manuscript.

Figure and Figure Caption

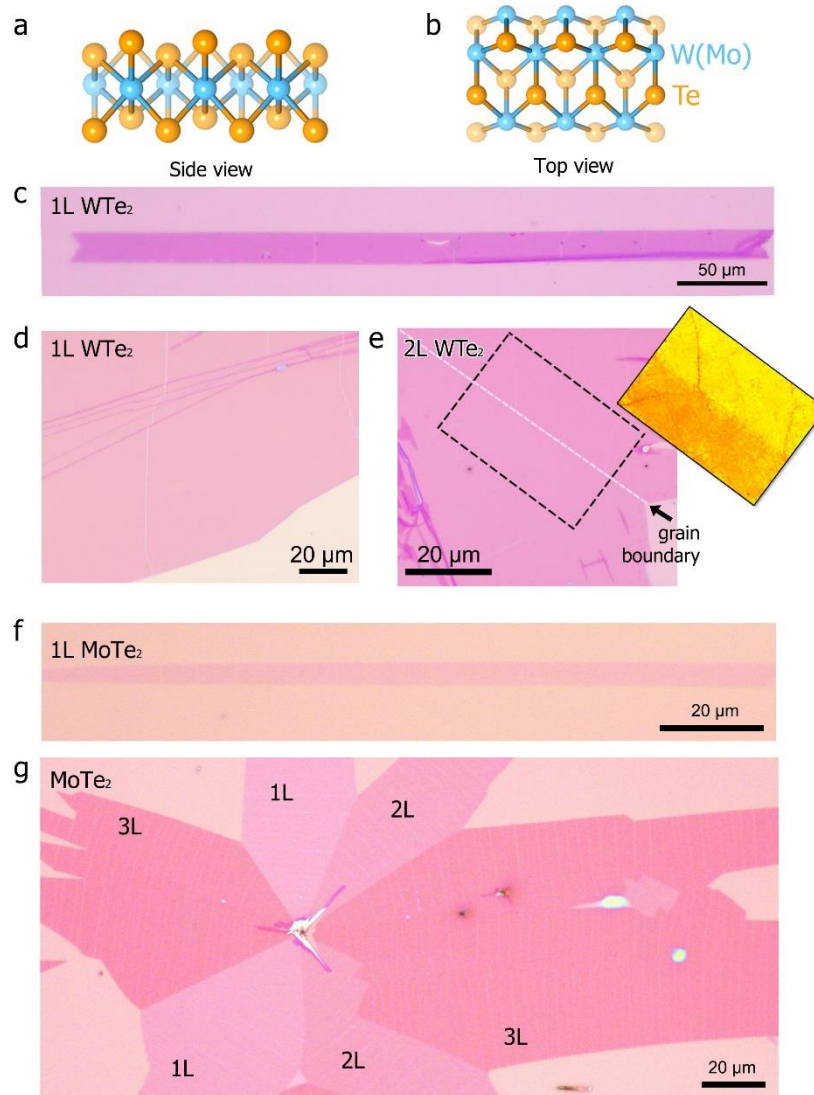


Fig.1. Optical geometries of WTe₂ and MoTe₂ monolayers. **a, b**, Side and top views of the crystal structure of 1T' W(Mo)Te₂, respectively. **c**, Optical image of a large single crystalline WTe₂ monolayer with a length of ~ 350 μm and width of ~ 20 μm. **d**, Optical image of a large WTe₂ monolayer film. **e**, Optical image of a large bilayer WTe₂ with grain boundary. The grain boundary is indicated by the arrow and the dashed line. Inset: false color image of the region indicated by the dashed rectangle, highlighting the location of the grain boundary. **f**, Optical image of a single crystalline MoTe₂ monolayer. With the length and width of ~ 150 and 8 μm, respectively. **g**, Optical image of a MoTe₂ flake containing 1L, 2L and 3L MoTe₂. The number of layer can be easily identified by their contrast.

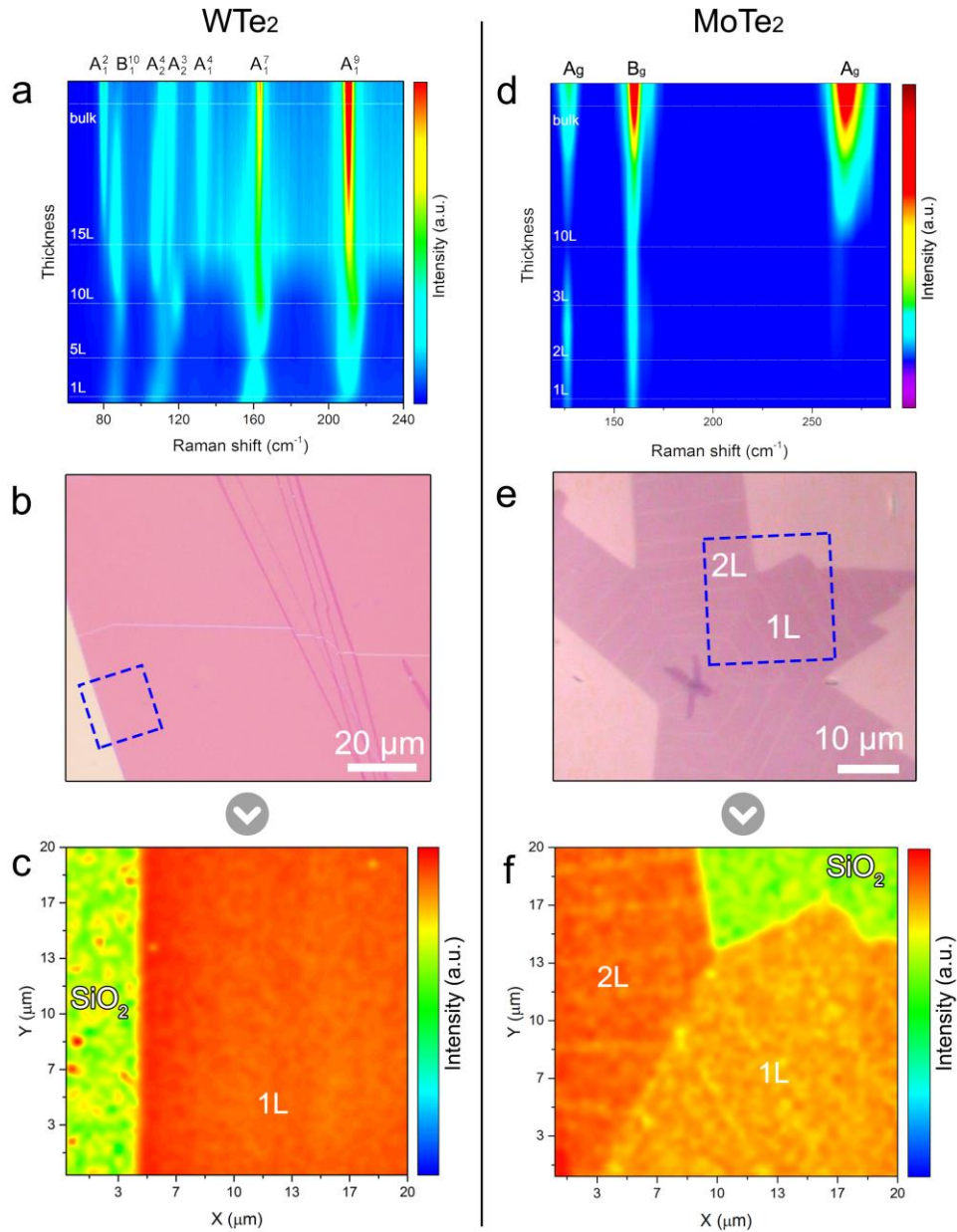


Fig.2. Raman spectra and mapping of WTe₂ and MoTe₂ monolayers. **a**, Thickness-dependent Raman spectra of WTe₂. Seven characteristic vibration modes are identified in bulk WTe₂ while only 4 of them can be observed in few-layer WTe₂. **b**, Optical image of a WTe₂ monolayer. **c**, Raman intensity mapping (from A_1^9) from the region (highlighted by blue dashed square) in **b**. The mapping size is $20 \times 20 \mu\text{m}$. The left side is SiO₂ while the right side shows a homogenous WTe₂ film. **d**, Thickness-dependent Raman spectra of MoTe₂. Four characteristic vibration modes are identified in bulk MoTe₂. Raman intensity dramatically decreases for all Raman peaks in MoTe₂ thin flakes. **e**, Optical image of MoTe₂ containing monolayer and bilayer regions. **f**, Raman intensity mapping (A_g @ 161 cm^{-1}) from the region highlighted by blue dashed square in **e**. The mapping size is $20 \times 20 \mu\text{m}$.

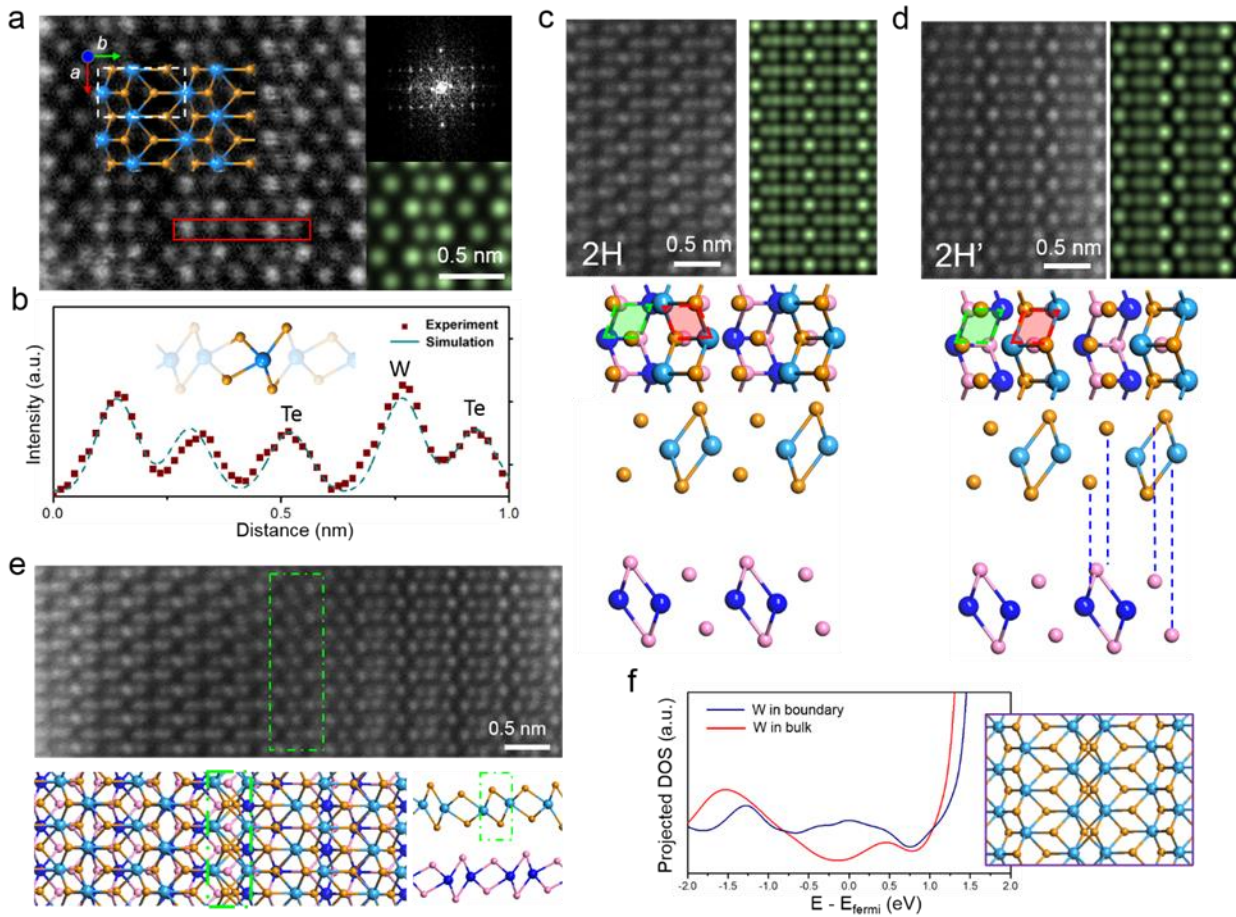


Fig.3. Atomic resolution STEM characterization of monolayer and bilayer WTe₂. **a**, STEM Z-contrast image of a monolayer WTe₂. The coordinate and structural model are overlaid on the image. Insets: FFT pattern and simulated STEM image of the monolayer WTe₂. **b**, Line intensity profile file of the region highlighted by red rectangle in **a**. **c**, **d**, STEM Z-contrast image of a bilayer WTe₂ with 2H stacking **c** and 2H' stacking **d**. The green and red dash diamonds indicate the orientation of the zigzag W-Te chains in the first and second layer, respectively. 2H and 2H' stacking is differed by half of a unit cell shifting along the *b* axis in the second layer. Images in green are simulated images. **e**, STEM Z-contrast image of an atomically sharp stacking boundary between the 2H (left) and 2H' (right) stacking. The structural model is optimized by DFT calculations. **f**, Projected DOS of the W atoms in the mirror twin boundary and in the bulk, showing more states near the Fermi level for W atoms in the boundary region. Inset: the structural model of the mirror twin boundary.

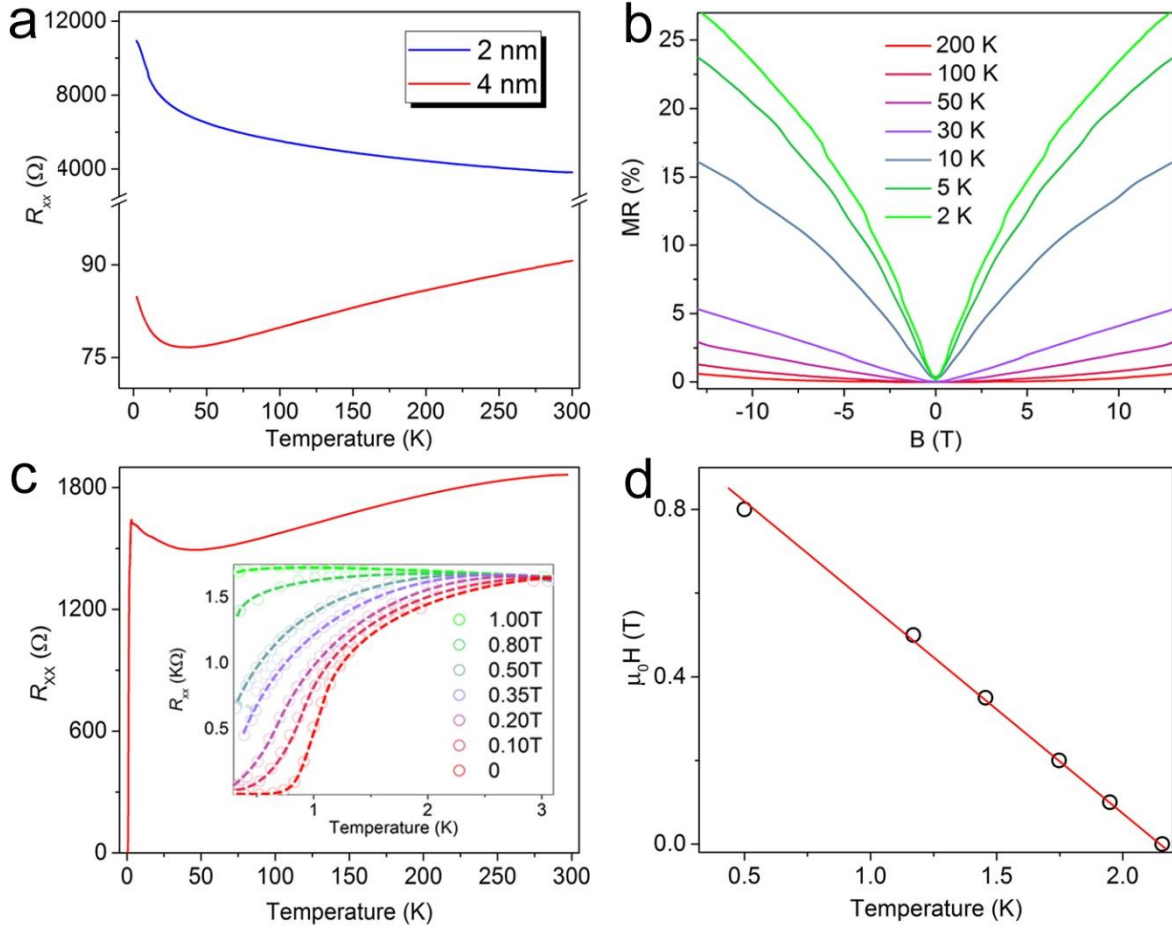


Fig.4. Transport in different thicknesses of WTe₂ and superconductivity in few layered MoTe₂. **a**, Temperature-dependent resistance of WTe₂ flakes with a thickness of 4 nm and 2 nm under zero magnetic field, respectively. The corresponding field dependent magnetoresistance of 2 nm WTe₂ flake at different temperatures is shown in **b**. WTe₂ shows a semimetal-to-insulator transition as the thickness decreased from 4 nm to 2 nm. **c**, Superconducting resistive transition of a few layered MoTe₂ at zero magnetic field. Inset: Superconductivity of the sample in different perpendicular magnetic fields. **d**, Temperature dependence of the upper critical field H_{c2} . The solid red line is the linear fit to H_{c2} .